Accurate 3D SMLM localization via Vectorial In-situ PSF Retrieval and Aberration Assessment

Xinxun Yang[1,5], Hongfei Zhu[2,5], Yile Sun[1], Hanmeng Wu[1], Yubing Han[1], Xiang Hao[1], Renjie Zhou[2], Cuifang Kuang[1,3,4,*] , Xu Liu[1,3,4]

[1] *State Key Laboratory of Extreme Photonics and Instrumentation, College of Optical Science and Engineering, Zhejiang University, Hangzhou, China, 310027*

[2]*Department of Biomedical Engineering, The Chinese University of Hong Kong, Hong Kong, China*

[3]*ZJU-Hangzhou Global Scientific and Technological Innovation Center, Hangzhou, Zhejiang 311200 China*

[4]*Collaborative Innovation Center of Extreme Optics, Shanxi University, Taiyuan, Shanxi 030006, China*

[5]*These authors contributed equally to this work*

[*]*Correspondence and requests for materials should be addressed to C.K. (e-mail: cfkuang@zju.edu.cn)*

Abstract

In single-molecule localization microscopy (SMLM) experiments, achieving precise localization results hinges on obtaining the authentic point spread function (PSF) influenced by system-induced and sample-induced aberrations. Here, we introduce VISPR (Vectorial in-situ PSF retrieval), a method employing the vector PSF model and the principles of maximum likelihood estimation (MLE). It facilitates the acquisition of an accurate PSF model under SMLM conditions, which faithfully represents system and sample-induced aberrations, relying solely on blinking raw data as input. This technique is capable of reconstructing the PSF with minimal error even in single-molecule data characterized by a very low signal-to-noise ratio. Consequently, the resulting PSF empowers accurate 3D super-resolution reconstruction in SMLM. Besides, we have observed that VISPR accurately retrieves high-frequency details of the authentic PSF across a significant depth range, a feat challenging for other approaches. As a result, this allows us to attain superior z-axis positioning accuracy across a broad z-axis range. In addition, VISPR is applicable to a variety of microscope modalities and can quantitatively assess aberrations induced by both the system and sample environment.

Introduction

In recent decades, super-resolution fluorescent microscopy techniques have become a crucial platform which surmounted the diffraction limit for exploring cellular structures including proteins, lipids, DNA, and RNA at the nanoscale. These technologies have played an important role in the development of the cell biology science. To be specific, Single Molecule Localization Microscopy (SMLM[1-3]), exemplified by techniques like PALM[2]/STORM[3], employs photo-switchable or blinking dyes and proteins to precisely detect and localize individual molecules, achieving sub-5nm precision in three dimensions[4, 5]. In 3D SMLM[6-11], the critical factor is the accurate knowledge of the Point Spread Function (PSF), enabling the precise localization and description of molecules with respect to its axial position within the specimen for 3D super-resolution imaging[12-14]. Besides, acquiring an accurate PSF holds significant importance for multiple applications, including the correction and analysis of aberrations introduced by the instrument and sample environment[15, 16], quantification and enhancement of microscopy system performance[17, 18], point spread functions (PSFs) engineering, such as double helix[8], phase ramp[19], or tetrapod[20], and the enhancement of SMLM positioning accuracy. Hence, it is crucial to attain an accurate PSF model that accounts for the impact of instrument imperfections and sample-induced aberrations arising from the non-uniform refractive indices within the sample.

To obtain the PSF model, current approaches rely on the calibrations generated from fiducial markers such as beads or gold nanoparticles[15, 21-26], which takes image stacks at various z-axis depths and subsequently utilizing phase retrieval algorithms for PSF retrieval. However, photons emitted by these fiducial markers never traverse the cellular or tissue sample, thus failing to consider aberrations induced by the sample environment, such as refraction mismatch caused by the photons passing through the complex biological and optical environment. Besides, the bead size ranges from 40 to 200 nm, significantly exceeding the size of a fluorophore molecule, which is approximately 2 nm. Therefore, the PSF model retrieved by beads has limitations when localizing in SMLM, such as heightened uncertainty in localization accuracy and resulting positional deviations in 3D.

Recently, Xu *et.al.* introduced INSPR generated directly derived from raw data in 3D SMLM using a modified Gerchberg-Saxton (GS) algorithm[27], which takes into account both the system-induced and sample-induced aberrations and is well-suited to the SMLM experimental conditions.

However, Xu's algorithm uses scalar PSF model, which is unsuitable for high numerical aperture (NA) microscope systems and causing model deviations during PSF generation. Simultaneously, the GS algorithm exhibits a high sensitivity to noise, rendering it unsuitable for data characterized by a low signal-to-noise ratio[28]. Furthermore, it incorporates an empirical Optical Transfer Function (OTF) scaling function in data processing[29], resulting in the omission of high-frequency information within the PSF spatial domain. This omission causes the generated PSF to gradually deviate from the authentic PSF as the depth axis increases. Additionally, this rescaling strategy lacks consistency in terms of phase restoration and cannot be theoretically supported or analyzed[28]. Therefore, the correctness of INSPR will be limited due to the deviation of the model, the suppression of PSF high-frequency information and sensitivity to background noise.

To accurately retrieve all parameters of a PSF model and solve the issues mentioned above, we draw inspiration from Xu's approach[27] and introduce the VISPR (Vectorial in-situ PSF retrieval), which is founded on a vectorial PSF model and Maximum Likelihood Estimation (MLE) phase estimation. In the article, we first introduce our method theoretically, including the introduction of the vector PSF model and the MLE algorithm. Subsequently, we employ both simulation experiments and practical experiments to validate the efficacy of VISPR. VISPR effectively addresses the issues in Xu's method where the PSF significantly deviates from the actual PSF position at considerable depths. As a result, it enhances the accuracy of three-dimensional PSF model restoration, yielding notably improved results. Furthermore, our methodology demonstrates robustness and is adaptable to a wide array of systems capable of conducting SMLM experiments.

Methods

Basic principles of VISPR

VISPR overcome the limitation in phase retrieval methods based on beads[15, 21-26] by directly retrieve the 3D PSF model from the raw single-molecule blinking dataset obtained from 3D SMLM experiments. The basic concept of 3D-SMILE is shown in Fig. 1. It consists of three major steps: 1) PSF library construction: segment the SMLM dataset into single-spot PSF library regarded as random axial distribution of the 3D PSF that we want to retrieve; 2) PSF library assignment: using an ideal vectorial PSF (Generated by a constant pupil and using vectorial PSF model) as reference PSF to assign the PSF library into classified PSFs based on the axial information with the aid of the mathematical frameworks of calculating the similarity between images; 3)3D PSF model estimation: these temporary axially assigned single-molecule spots are assembled, aligned and averaged to form a 3D PSF stack. Then we use maximum likelihood estimation (MLE) phase retrieval to estimate the new pupil and Zernike coefficients of the PSF stacks. This new pupil generates an updated vectorial reference template and steps 2-3 are repeated. For data with low signal-to-noise ratio (SNR), 6-10 iterations are required to converge. To avoid the degeneracies occurred during the process mentioned in HF, we use the prior knowledge of the astigmatism orientation to generate asymmetric reference PSF, which helps us to build the unique in situ vectorial PSF model.

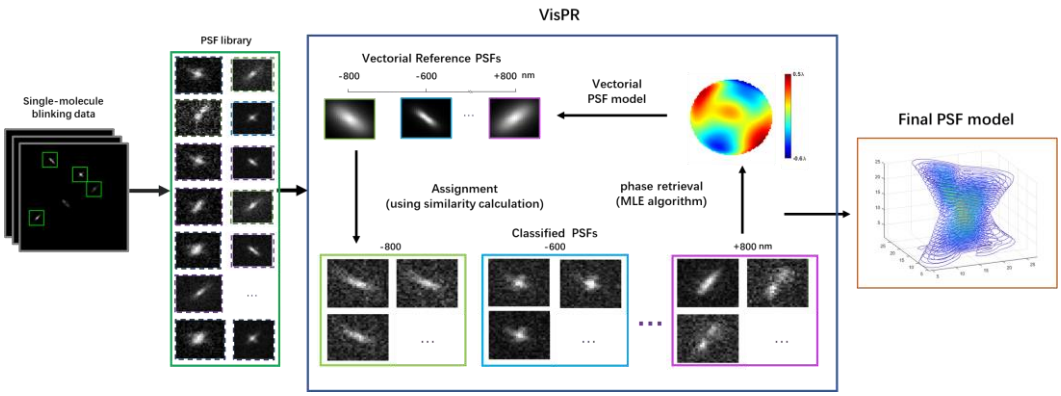

Figure 1. Concept of VISPR. After the single-molecule dataset (left) is acquired by SMLM experiments, a PSF library is obtained by segmentation. VISPR uses a starting pupil function with constant Zernike coefficients to obtain the reference vector PSF stacks. Then the reference PSF stacks assigns each emitter patterns to different z-axis positions according to its similarity with the template. These axially assigned PSFs are subsequently grouped, aligned and averaged to form a 3D PSF stack, which is then used to estimate the PSF model using MLE phase retrieval. The new pupil generates an updated reference vectorial PSF model for next iteration. This process iterates about 6-8 times to converge and get the final PSF model.

Point spread function models

A. Scalar PSF Model

For optical system with low numerical aperture (NA), the intensity profile in the focal plane and the complex signal in the pupil plane are simply related via the Fourier transform, as described as the Fresnel approximation[28]. A necessary condition for the validity of the Fresnel approximation is that the effect of light polarization on the diffracted images is negligible. The scalar PSF model can be related to the wavefront aberration $\phi(x)$ as

$$PSF_s \propto \left|\mathcal{F}_{2D}\left\{A(\rho,\varphi)\cdot e^{j(\phi_{pos}(\rho,\varphi,x_0,y_0)+\phi_{ab}(\rho,\varphi,x_0,y_0,z_0))}\right\}\right|^2 \tag{1}$$

Where $\mathcal{F}_{2D}$ is the 2D Fourier transform, $(\rho,\varphi)\in\mathbb{R}^2$ is the normalized polar coordinate in the back focal plane (BFP). (x_0,y_0,z_0) is the 3D position of the point source in the sample plane. PSF_s is the intensity of the optical field in the focal plane, A is the amplitude of the pupil plane. $\phi_{pos}(\rho,\varphi,x_0,y_0,z_0)$ indicates the phase shift correlated with the emitter position and objective position, which is defined as:

$$\phi_{pos}(\boldsymbol{x}) = \frac{2\pi}{\lambda}\left(x_0k_x + y_0k_y + z_0k_z\right), \tag{2}$$

With

$$k_z = \sqrt{1-k_x^2-k_y^2} \tag{3}$$

Where λ is the wavelength, and (k_x,k_y) are the x and y components of the unit wave vector. $\phi_{ab}(\boldsymbol{x})$ represents the field-dependent aberrations and is expressed as a liner sum of variance normalized Zernike polynomials:

$$\phi_{ab}(\boldsymbol{x}) = \sum\nolimits_{n+|m|\le 8} C_n^m(\boldsymbol{x})\cdot Z_n^m(\boldsymbol{u}) \tag{4}$$

Where C_n^m is the aberration coefficients, Z_n^m is the normalized Zernike polynomial, n is the radial order and m is the angular frequency.

B. Vectorial PSF Model

The scalar PSF model only focuses on the Fourier transform relationship between pupil and PSF according to the Fresnel approximation, while ignores the vector nature of light, which is applicable in low-NA situations. However, for high-NA optical systems[30] (e.g., NA ≥ 0.6), the vector nature of light cannot be neglected because the bending of the rays created by a lens introduces a significant z component of the electromagnetic field in the region behind the lens. We can model the PSF according to the vector theory of diffraction[31] by considering the x, y, z components of the

field right after the lens separately for polarization vector with x and y components. We consider that each volume element of the sample represents an ensemble of independently emitting fluorophore molecules, which we described as uncorrelated dipole radiators (with random orientations) which can rotate or wobble freely. The PSF are treated as the summed image of three orthogonal dipoles: x, y, z directions. Thus, our calculation of the vectorially PSF simply consists of calculating and adding six intensity PSFs incoherently which is modulated by six field vectorial coefficients:

$$PSF_v \propto \sum_{p=x,y} \sum_{d=x,y,z} \left|\mathcal{F}_{2D}\left\{A'(\rho,\varphi) \cdot e^{j(\phi_{pos}(\rho,\varphi,x_0,y_0)+\phi_{ab}(\rho,\varphi,x_0,y_0,z_0))} \cdot E_{p,d}\right\}\right|^2 \quad (5)$$

with

$$A'(\rho,\varphi) = A(\rho,\varphi)/\sqrt{cos\theta} \quad (6)$$

Where $A'(\rho,\varphi)$ indicates the amplitude function with obliquity factor. And the six coefficients $E_{p,d}$ represent the polarization vectors of electrical field with components $p = x, y$ in the image plane with orthogonal dipole components $d = x, y, z$ contributes to components p :

$$E_{x,d} = T_p\overrightarrow{P_d}\, cos\varphi - T_s\overrightarrow{S_d} sin\varphi \quad (7a)$$

$$E_{y,d} = T_p\overrightarrow{P_d}\, sin\varphi + T_s\overrightarrow{S_d}\, cos\varphi \quad (7b)$$

$$with \left(\vec{P} = \begin{bmatrix} cos\theta_{med} cos\varphi \\ cos\theta_{med} sin\varphi \\ -sin\theta_{med} \end{bmatrix}, \vec{S} = \begin{bmatrix} -sin\varphi \\ cos\varphi \\ 0 \end{bmatrix}\right). \quad (7c)$$

Here $\vec{P}$ and $\vec{S}$ are the light field polarization vectors. T_p and T_s are the Fresnel transmission coefficients for p and s polarization. The six field components can be used to calculate the total electrical field energy at any point after the lens; in particular, they determine the intensity seen by an imaging plane in any orientation.

MLE phase retrieval algorithm

MLE is an effective method to fit Poisson distribution models. We know that the measurement noise of the camera along pixels is independent and identically distributed with Poisson function, so the PSF intensity profile on the camera is also Poisson distributed, which can be accurately fitted by MLE especially for low signal-to-noise conditions.

The proper procedure with MLE phase retrieval is to adjust fitting parameters to minimize the MLE for the Poisson distribution. We use the L-M algorithm[24] to minimize the maximum-likelihood based loss-function given by

$$\chi_{MLE}^2 = 2\left(\sum_k (f_k - x_k) - \sum_{k,x_k>0} x_k \ln(f_k/x_k)\right) \tag{8}$$

Where f_k is the expected number of photons in pixel k from the model PSF function with parameters, and x_k is the measured number of photons in raw data. This function is minimized to find the maximum likelihood for the Poisson process.

Microscope setup

To implete and validate the proposed algorithm, we built a customized SMLM system based on adaptive optics. By going through an optical coupler (Schäfter + Kirchhoff GmbH, 60SMS-1-4-RGBV11-47), the single-wavelength Laser was coupled into a single-mode optical fiber (Schäfter + Kirchhoff GmbH, PMC-E-400RGB-3.5-NA011-3-APC.EC-350-P) and then collimated by a beam collimator (Schäfter + Kirchhoff GmbH, 60FC-T-4-M25-01). after the module of fiber optics, the beam propagated to a 200-mm tube lens (Thorlabs, TTL200-A) with relay of a 4f system which adjusted the illumination area and made the pixel size to be 89 nm. Through the tube lens, the excitation beam was focused to the back focal plane of an oil-immersion objective lens (Olympus, UPLXAPO100XO).) and formed epi-illumination. The fluorescence of each single molecule was collected by objective lens and passed to a deformable mirror (Boston Micromachines Corporation, Multi-3.5L-DM). it should be noted that the surface of deformable mirror conjugated with back focal plane and can be relayed by 4f configuration. Finally the pupil was focused by a doublet lens (Thorlabs, AC254-125-A-ML) and the single-molecule raw images were collected by a scientific CMOS (Hamamatsu, ORCA-FusionBT C15440-20UP).

Sample preparation

For 40nm-bead samples, we used the dark red fluorescent FluoSpheres beads (F8801) for fluorescent bead samples which were maximally excited at 589 nm. Dilute the beads in ultrapure water at a ratio of 1:10000, and vibrate in an ultrasonic cleaner for 5 mins. Next, 200 μl of the diluted beads were placed on a coverslip and allowed to stand for 10 mins. The absorbent tissue was then used to remove excess water and Prolong GlassDiamond Antifade (Thermo Fisher Scientific, Inc.) before sealing the coverslip.

Results

Simulation Verification

We validated and tested the feasibility of our VISPR extensively with single molecule simulations. Specifically, we generated a single-molecule randomly blinking dataset (Fig. 2a) based on the cubic-spline representation of a ground truth vectorial astigmatic PSF model with a set of Zernike aberrations consisted of 21 Zernike modes (Noll order) and random axial range of ± 800nm. Each molecule was then be added with a constant background and finally degraded by Poisson noise. In simulated experiments, we found that VISPR successfully estimated the ground truth pupil (Fig. 2b) with error in 13nm (the root-mean-square (RMS) error of the wavefront) and the correct Zernike amplitude coefficients with error in 11nm for the total 21 modes (Fig. 2c).

Next, we compare the results of VISPR with INSPR[27]. In the simulation experiment, we observed that in the -400-+400nm region, both INSPR and VISPR have a high degree of similarity with the real PSF (Fig. 2D). However, as the z-axis depth increases to more than ±400nm, the INSPR PSF model will generate considerable distortions that is visible to the naked eye compared to the VISPR PSF. The 3D PSF fitted by VISPR shows a linear relationship with the real PSF between the fitted z-position and the objective z-position, whereas INSPR resulted in a distortion, suggesting a mismatch of the PSF model from the data. Furthermore, we three-dimensionally reconstructed the simulated single-molecule datasets with real 3D PSF, INSPR PSF, and VISPR PSF separately. We then evaluated both localization precision and accuracy in 3D at different axial positions from 100 simulated molecules at each axial position to demonstrate the performance of VISPR and INSPR. The *localization precision* is calculated as the standard deviation of the difference between the fitted positions and ground truth positions, and the *localization accuracy* is calculated as the root mean square error between the fitted positions and ground truth positions. Fig. 2e shows that the evaluated x, y, z positions results localized by VISPR-retrieved 3D PSF model showed excellent similarity with the ground truth of the simulated data with only 500 single molecules (4000 total photons/localization, 10 background photons per pixel, z-range -600 nm to 600 nm). However, there will be a large deviation between the x, y, and z positions located by INSPR and real PSF. At the same time, we can find that the mean z position of INSPR positioning in the -400 to 400nm region is close to the real PSF, but after exceeding the 400nm range, there will be a large deviation from the real PSF. Besides, we further verified the performance of VISPR under low signal-to-noise ratio

circumstance considering the situation of conventional single-molecule experiments. We found that even when the signal-to-noise ratio is as low as 2:1 (2000 total photons, 80 background photons per pixel, z-range -600 nm to 600 nm), the estimated pupil can still reach a value below 33nm (the root-mean-square (RMS) error of the wavefront), and if the number of input single molecules is increased to 1000 molecules, the estimated pupil will reach higher accuracy: less than 20nm.

Furthermore, we used VISPR and INSPR to reconstruct the simulated microtubule structure respectively. The ground truth of the microtubules was obtained from the EPFL 2016 SMLM Challenge training data set (http://bigwww.epfl.ch/smlm). Firstly, we use a ground truth vectorial astigmatic PSF model to generate the simulated single-molecule dataset. Then, we input the dataset of microtubules into VISPR and INSPR, and then used the 3D PSF model retrieved separately to reconstruct the microtubule super-resolution image. From the results, we can see that in the -300 to 300nm region (Fig. 3c,i), the x-z reconstruction results of VISPR and INSPR are close to the real values. However, as the depth increases, the z-axis position of INSPR will deviate from the Ground truth, while the results of VISPR still can fit well and is close to the Ground truth (Fig. 3f,k), which further illustrates the effectiveness of VISPR which enables the blind super-resolution reconstruction of aberrated SMLM datasets.

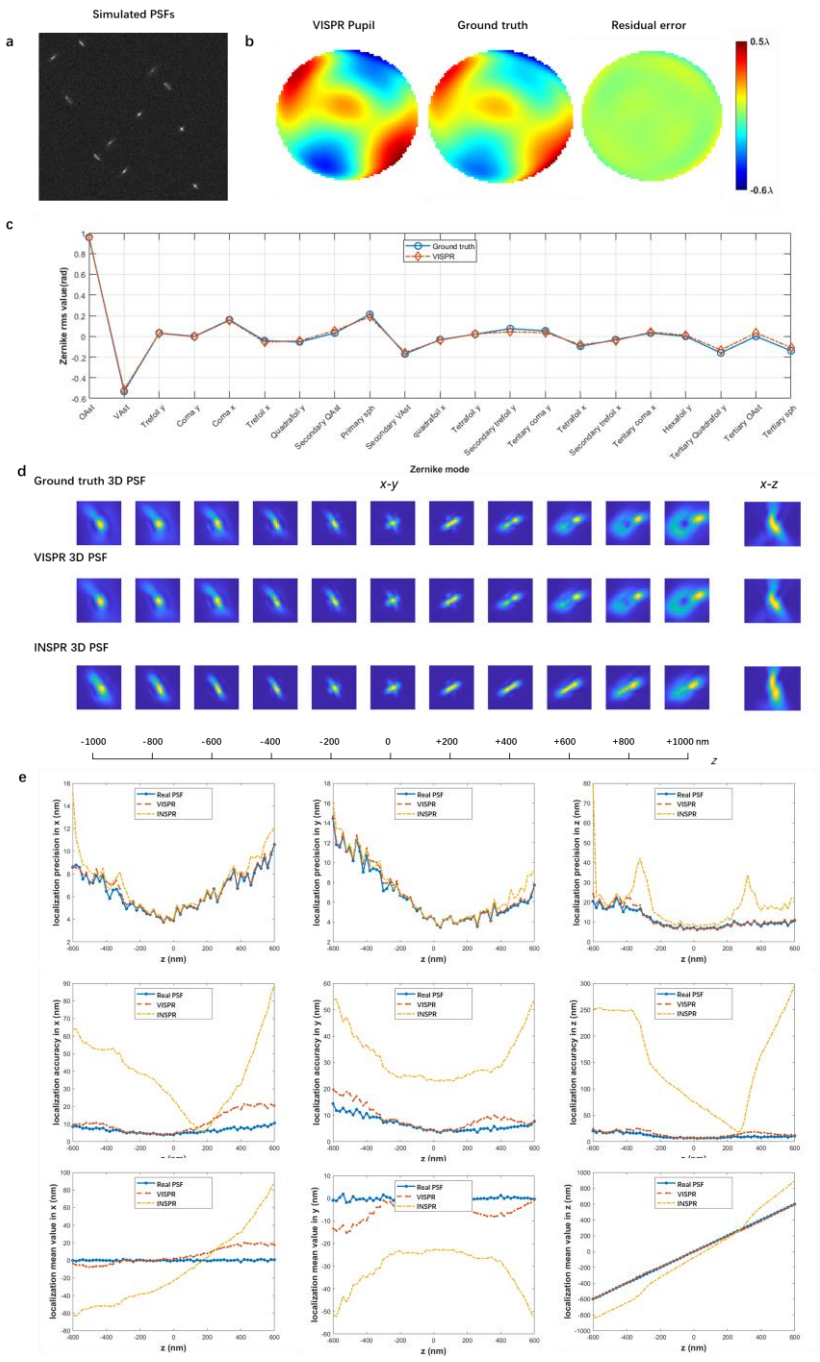

Figure 2. Performance quantification of VISPR on simulations. **a,** Simulated single-molecule dataset located randomly over an axial range from –800 to +800 nm with a known PSF model. **b,** Phase of the VISPR pupil (left), the ground truth pupil (middle) and the residual error (right). The RMSE is 11.33 nm. **c,** Coefficients of 21 Zernike modes retrieved by VISPR compared with the ground truth (red circles). **d,** x–y and x–z views of the Ground truth 3D PSF (top row), VISPR-retrieved 3D PSF (middle row), INSPR-retrieved PSF (bottom raw). In the -400 to 400nm region, VISPR and INSPR are very similar to the real PSF. However, in the region beyond the z-axis 400nm, INSPR shows a serious deviation from the real PSF due to the lack of high-frequency information, while VISPR still maintains high similarity with the real PSF. **e,** Localization precision, accuracy and mean value in x, y, z positions at different axial positions with real PSF, VISPR and INSPR.

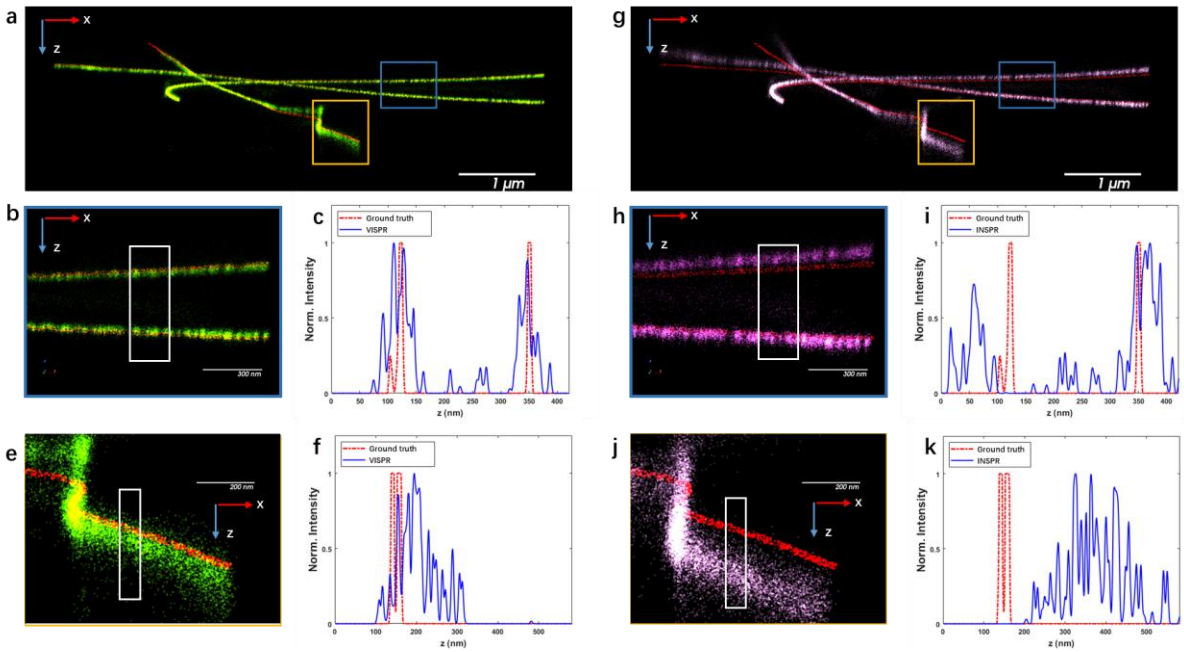

Figure 3. Comparison the effectiveness of blind reconstruction of 3D SMLM microtubules between VISPR and INSPR. a,g, x-z overviews of the simulated microtubules resolved by VISPR and INSPR from the 3D SMLM data. **b,e,** Enlarged x-z views of the areas as indicated by the blue and orange boxed regions in (a) , respectively. **c,f,** Intensity profiles along the z directions within the white boxed regions in (b,e), comparing the VISPR resolved profiles (blue solid lines) with the ground truth (red dashed lines). **h,j,** Enlarged x-z views of the areas as indicated by the blue and orange boxed regions in (g) , respectively. **i,k,** Intensity profiles along the z directions within the white boxed regions in (h,j), comparing the INSPR resolved profiles (blue solid lines) with the ground truth (red dashed lines).

Experimental Verification

To evaluate the performance of VISPR, experiments on 100 nm fluorescent nanospheres were conducted as a proof of concept, which were settled on the upper surface of the cover slip. We added a vertical astigmatism-dominant aberration with other random but non-primary Zernike coefficients to the imaging system (Fig. 4b). The validation experiment was divides into three parts: 1), We staged and captured the beads from -600 to 600 nm with a 50 nm step. The average of stacks of bead candidates with high photon intensity within the field of view (FOV) was utilized for in-vitro PSF/pupil retrieval using vectorial model and MLE fitting. This PR PSF and pupil were regarded as the ground-truth of the system; 2), We staged and captured the beads from -600 to 600 nm with a random step interval, i.e., the step sizes range from 2 to 7 nm randomly, to mimic in-situ SMLM raw data (Fig. 4c). VISPR and INSPR method were applied to get the in-situ PSF model and pupil function, respectively. It can be seen that in Fig.4a, both PR and VISPR can accurately retrieve the shape of the beads. In contrast, the shape of INSPR PSF model at large depths (>300nm) deviates greatly from the PR PSF and real beads, because INSPR cannot retrieve the high-frequency information of the beads image; 3) We captured 50 repeated bead images for each depth from -600 to 600 nm with a 50 nm step. For each bead candidate in the FOV, PR PSF, VISPR PSF and INSPR PSF models were utilized to fit the 3D coordinates at each depth, and the average values of $x/y/z$ coordinates of the PR PSF result at each depth were regarded as the ground-truth coordinates for this specific bead candidate. The localization precision $\Delta x/\Delta y/\Delta z$ as well as the corresponding localization accuracy (mean square error relative to the ground-truth coordinates) of PR/VISPR/INSPR fitting at each depth was calculated. It should be noted that for the VISPR/INSPR localization results, we added a global 3D displacement to the original fitting coordinates to compensate for the displacement offset between PR PSF and VISPR/INSPR PSF model. This is reasonable because the translation of the 3D reconstruction does not affect the final structural information. In Fig. 4d, we showed the comparison of the z axis localization precision and accuracy of two bead (the white boxed regions in Fig. 4b) candidates using PR/VISPR/INSPR respectively. The comparison of the x/y axis localization precision and accuracy is placed in the supplementary materials. Due to the random jitter of the sample stage, the z-position the beads in the same z-axis area will also deviate, which will cause fluctuations in precision and accuracy. However, through the comparison of precision, accuracy and mean value at different z-axis positions, we still find that

the average positions of VISPR and PR on the z-axis positioning can correctly reflect the movement of the stage and VISPR performs better in precision and accuracy. In contrast, the position of INSPR produce obvious deviations from the PR PSF, which illustrates the limitations of INSPR.

We also conducted in-situ experiments with other types of aberrations. i.e., oblique astigmatism-dominant aberration with other random but non-primary Zernike coefficients. VISPR showed better performance than INSPR and was close to reaching the Cramér-Rao lower bound (CRLB) under different aberration conditions.

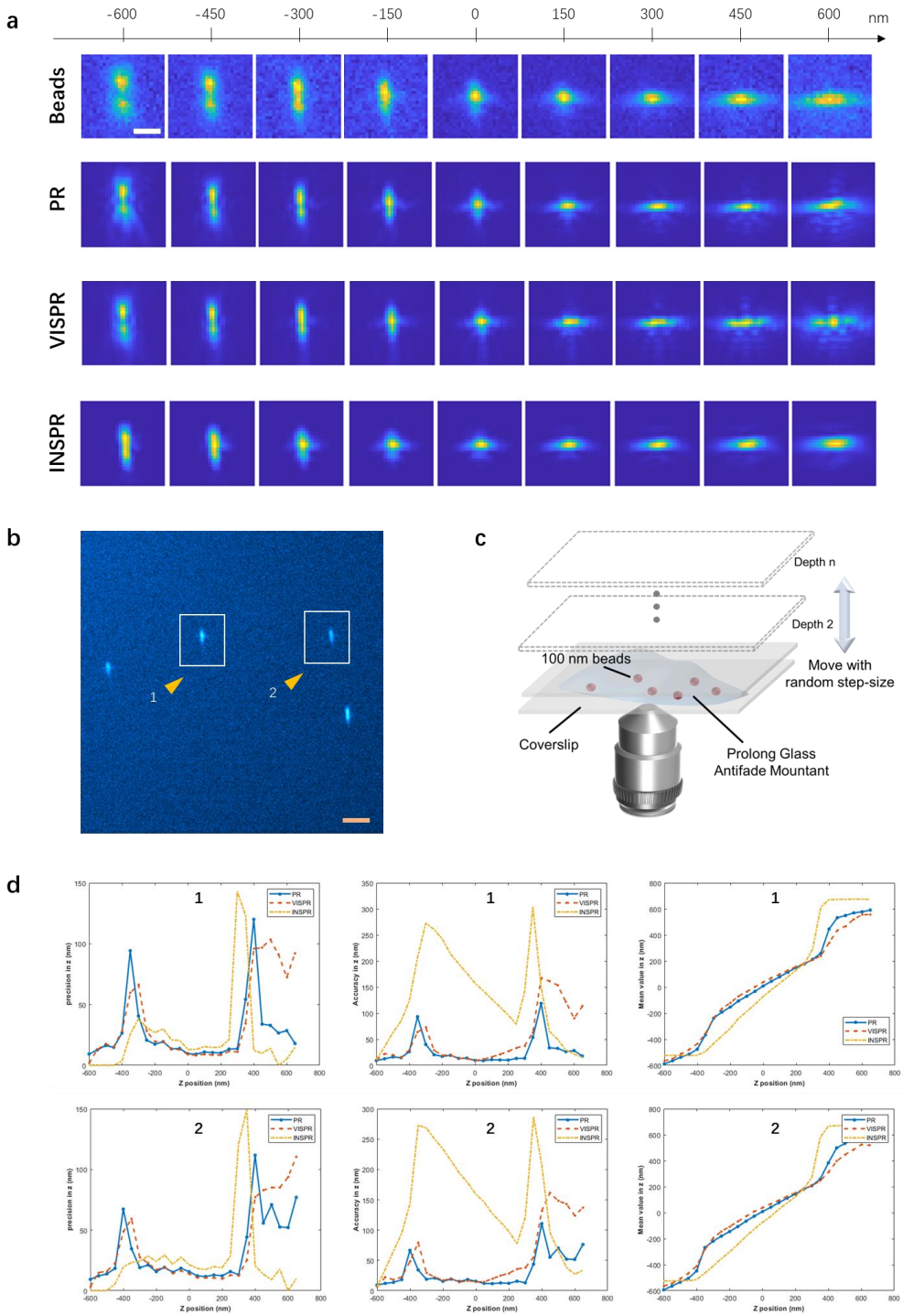

Figure 3. Experimental validation of VISPR. a, The original data of beads, the PSF obtained by PR, the PSF obtained by VISPR, and the PSF obtained by INSPR are presented at different z-axis depths. **b,** Partial FOV showing the sample with sparse single beads. The localization precision, accuracy and mean value of the beads pointed by the yellow arrows are measured. **c,** A sketch of the sample used to measure localization precision at different depth. The 100 nm particles are on the upper surface of the cover slip and moved by a Piezo stage to different axial depths. **d,** Localization precision, accuracy and mean value curve across the depth of field of the two candidate molecules. Scale bars: 2 um for **b** and 500 nm for others.

4. Conclusion

We developed VISPR, an effective in-situ phase retrieval framework that can directly retrieve 3D PSF models from raw single-molecule datasets and accurately position single molecules in three dimensions, in the presence of both system and sample-induced aberrations. We verify it through simulations data sets and experiments. In the simulation experiment, we verified that VISPR has higher fitting ability than INSPR owing to the improvement of the model and algorithm, and there will be no distortion in the recovery of 3D PSF model at large depths compared to the INSPR. With the help of vectorial PSF model and MLE phase retrieval algorithm, VISPR is able to solve the model deviation and the problem of missing high-frequency information at large depths in the z-axis. VISPR relies on single-molecule data within a certain z-axis range, so if most of the single-molecule data are at the same z-axis position VISPR may fail.

For SMLM data at large depths such as intra- and extracellular cellular targets deep inside tissues, phase retrieval based on beads cannot reflect the real PSF well, because many biological samples contain strong variations in refractive index which cannot be observed in the case of beads. In that case, VISPR can robustly and accurately restore the 3D PSF model because it considers aberrations caused by the system and sample at the same time. Besides, VISPR improves the accuracy of the PSF model by solving the problem of PSF model distortion at large depths and it is applicable to low signal-to-noise ratio SMLM situations, which provide critical guidance for optimizing the subsequent optical system performance, correcting and analyzing aberrations caused by the system and samples, estimating the properties of single molecules, and increasing imaging contrast and resolution.

Code availability

Data underlying the results presented in this paper are not publicly available at this time but may be obtained from the authors upon reasonable request.

Author contributions

X.Y., H.Z. and Y.S. conceived and initiated the project. X.Y., H.Z. and Y.S. designed and built the optical system. X.Y. wrote the software control code. X.Y., H.Z., Y.S. and H.W. designed and performed simulations and experiments. X.Y., H.Z. analyzed the data. X.Y., Y.S. and H.W prepared the experimental samples. X.Y., and H.Z., wrote the article. C.K. and X.L. guided and supervised the whole project. All authors wrote the paper and contributed to the scientific discussion and revision of the article.

Funding

National Natural Science Foundation of China (62125504, 61827825); STI 2030—Major Projects (2021ZD0200401); Major Program of the Natural Science Foundation of Zhejiang Province (LD21F050002); Zhejiang Provincial Ten Thousand Plan for Young Top Talents (2020R52001). Open Project Program of Wuhan National Laboratory for Optoelectronics (2021WNLOKF007)

Competing financial interests

The authors declare no competing interests.

References

1. E. Betzig, G. H. Patterson, R. Sougrat, O. W. Lindwasser, S. Olenych, J. S. Bonifacino, M. W. Davidson, J. Lippincott-Schwartz and H. F. Hess, Science **313** (5793), 1642-1645 (2006).
2. S. T. Hess, T. P. Girirajan and M. D. Mason, Biophys J **91** (11), 4258-4272 (2006).
3. M. J. Rust, M. Bates and X. Zhuang, Nature Methods **3** (10), 793-796 (2006).
4. F. Huang, G. Sirinakis, E. S. Allgeyer, L. K. Schroeder, W. C. Duim, E. B. Kromann, T. Phan, F. E. Rivera-Molina, J. R. Myers, I. Irnov, M. Lessard, Y. Zhang, M. A. Handel, C. Jacobs-Wagner, C. P. Lusk, J. E. Rothman, D. Toomre, M. J. Booth and J. Bewersdorf, Cell **166** (4), 1028-1040 (2016).
5. T. Schlichthaerle, M. T. Strauss, F. Schueder, A. Auer, B. Nijmeijer, M. Kueblbeck, V. Jimenez Sabinina, J. V. Thevathasan, J. Ries, J. Ellenberg and R. Jungmann, Angew Chem Int Ed Engl **58** (37), 13004-13008 (2019).
6. M. F. Juette, T. J. Gould, M. D. Lessard, M. J. Mlodzianoski, B. S. Nagpure, B. T. Bennett, S. T. Hess and J. Bewersdorf, Nat Methods **5** (6), 527-529 (2008).
7. B. Huang, W. Wang, M. Bates and X. Zhuang, Science **319** (5864), 810-813 (2008).
8. S. R. Pavani, M. A. Thompson, J. S. Biteen, S. J. Lord, N. Liu, R. J. Twieg, R. Piestun and W. E. Moerner, Proc Natl Acad Sci U S A **106** (9), 2995-2999 (2009).
9. D. Aquino, A. Schönle, C. Geisler, C. V. Middendorff, C. A. Wurm, Y. Okamura, T. Lang, S. W. Hell and A. Egner, Nat Methods **8** (4), 353-359 (2011).
10. P. Bon, J. Linarès-Loyez, M. Feyeux, K. Alessandri, B. Lounis, P. Nassoy and L. Cognet, Nat Methods **15** (6), 449-454 (2018).
11. D. Sage, T. A. Pham, H. Babcock, T. Lukes, T. Pengo, J. Chao, R. Velmurugan, A. Herbert, A. Agrawal, S. Colabrese, A. Wheeler, A. Archetti, B. Rieger, R. Ober, G. M. Hagen, J. B. Sibarita, J. Ries, R. Henriques, M. Unser and S. Holden, Nat Methods **16** (5), 387-395 (2019).
12. A. Small and S. Stahlheber, Nat Methods **11** (3), 267-279 (2014).
13. E. Nehme, L. E. Weiss, T. Michaeli and Y. Shechtman, Optica **5** (4), 458-464 (2018).
14. P. Zhang, S. Liu, A. Chaurasia, D. Ma, M. J. Mlodzianoski, E. Culurciello and F. Huang, Nat Methods **15** (11), 913-916 (2018).
15. D. Burke, B. Patton, F. Huang, J. Bewersdorf and M. J. Booth, Optica **2** (2) (2015).
16. Y. Li, Y.-L. Wu, P. Hoess, M. Mund and J. Ries, Biomedical Optics Express **10** (6), 2708-2718 (2019).
17. P. Theer, C. Mongis and M. Knop, Nature Methods **11** (10), 981-982 (2014).
18. O. Faklaris, L. Bancel-Vallée, A. Dauphin, B. Monterroso, P. Frère, D. Geny, T. Manoliu, S. de Rossi, F. P. Cordelières, D. Schapman, R. Nitschke, J. Cau and T. Guilbert, J Cell Biol **221** (11) (2022).
19. D. Baddeley, M. Cannell and C. Soeller, Nano Research **4**, 589-598 (2011).
20. Y. Shechtman, S. J. Sahl, A. S. Backer and W. E. Moerner, Phys Rev Lett **113** (13), 133902 (2014).
21. M. Siemons, C. N. Hulleman, R. Ø. Thorsen, C. S. Smith and S. Stallinga, Optics Express **26** (7), 8397-8416 (2018).
22. S. Liu, E. B. Kromann, W. D. Krueger, J. Bewersdorf and K. A. Lidke, Optics Express **21** (24), 29462-29487 (2013).
23. P. N. Petrov, Y. Shechtman and W. E. Moerner, Opt Express **25** (7), 7945-7959 (2017).
24. Y. Li, M. Mund, P. Hoess, J. Deschamps, U. Matti, B. Nijmeijer, V. J. Sabinina, J. Ellenberg, I. Schoen and J. Ries, Nature Methods **15** (5), 367-369 (2018).
25. E. Goi, S. Schoenhardt and M. Gu, Nature Communications **13** (1), 7531 (2022).

26. A. Aristov, B. Lelandais, E. Rensen and C. Zimmer, Nat Commun **9** (1), 2409 (2018).
27. F. Xu, D. Ma, K. P. MacPherson, S. Liu, Y. Bu, Y. Wang, Y. Tang, C. Bi, T. Kwok, A. A. Chubykin, P. Yin, S. Calve, G. E. Landreth and F. Huang, Nature Methods **17** (5), 531-540 (2020).
28. N. Hieu Thao, O. Soloviev and M. Verhaegen, J. Opt. Soc. Am. A **37** (1), 16-26 (2020).
29. B. M. Hanser, M. G. Gustafsson, D. A. Agard and J. W. Sedat, J Microsc **216** (Pt 1), 32-48 (2004).
30. J. J. M. Braat, P. Dirksen, A. J. E. M. Janssen, S. van Haver and A. S. van de Nes, J. Opt. Soc. Am. A **22** (12), 2635-2650 (2005).
31. M. Mansuripur, *Classical Optics and its Applications*, 2 ed. (Cambridge University Press, Cambridge, 2009).